Edinburgh Research Explorer

Accessing the soot-related radiative heat feedback in a flame spreading in microgravity: optical designs and associated limitations

Accessing the soot-related radiative heat feedback in a flame spreading in microgravity: optical designs and associated limitations

A. Guibaud[a], J.-M. Citerne[a], J.-L. Consalvi[b], J.L. Torero[c], O. Fujita[d],
M. Kikuchi[e], P. Ferkul[f], N. Smirnov[g], G. Jomaas[h], B. Toth[i], S. Rouvreau[j],
G. Legros[a,*]

[a]*Centre National de la Recherche Scientifique, Sorbonne Université, UMR 7190, Institut Jean Le Rond d'Alembert, Paris F-75005, France*
[b]*Aix-Marseille Université, IUSTI/UMR CNRS 7343, 5 rue E. Fermi, 13453 Marseille Cedex 13, France*
[c]*Department of Civil, Environmental and Geomatic Engineering, University College London, Gower Street, London, WC1E 6BT, UK*
[d]*Hokkaido University, Sapporo, Japan*
[e]*Japan Aerospace Exploration Agency, 2-1-1 Sengen, Tsukuba, Ibaraki 305-8505, Japan*
[f]*NASA Glenn Research Center, 21000 Brookpark Rd., Cleveland, OH 44135, USA*
[g]*Lomonosov Moscow State University, and Federal Science Center, NIISI Russian Academy of Sciences, Moscow, Russia*
[h]*School of Engineering, University of Edinburgh, Edinburgh, UK*
[i]*ESA ESTEC, Noordwijk, Netherlands*
[j]*Belisama R&D, Toulouse, France*

Abstract

Novel, high-fidelity results related to soot from microgravity flames were obtained by an international topical team on fire safety in space. More specifically, embedded optical techniques for evaluation of the soot-related radiative feedback to the base material from a spreading non-premixed flame in microgravity were developed. The configuration used a non-buoyant axisymmetric flame propagating in an opposed laminar stream over a Low Density

*Corresponding author:
    Email address:* `guillaume.legros@sorbonne-universite.fr` *(G. Legros)*

PolyEthylene coating of an electrical wire. Within this context, both the standard Broadband Two Color Pyrometry (B2CP) and its recent extension Broadband Modulated Absorption/Emission (BMAE) technique can be deployed to measure the spatial distribution of soot temperature and volume fraction within the flame. Both fields are then processed to establish the field of local radiative balance attributed to soot within the flame, and ultimately the soot contribution to the radiative flux to the wire. The present study first assesses the consistency of the methodology contrasting an experimental frame and a synthetic one, the latter being produced by a signal modeling that processes fields delivered by a numerical simulation of the configuration as inputs. Using the synthetic signals obtained, the fields of local radiative balance within the flame are then computed and significant discrepancies were disclosed locally between the fields originating from the synthetic BMAE and B2CP inputs. Nevertheless, the subsequent evaluation of the soot-related radiative heat feedback to the wire shows that a weak deviation among the techniques implemented is expected. This finding is corroborated by similar evaluations conducted with experimental BMAE and B2CP measurements obtained in parabolic flights. As BMAE is implemented in an ISS configuration within the SCEM rig, BMAE and B2CP will soon provide long-duration soot observations in microgravity. In order to contrast the upcoming results, this current study quantifies discrepancies originating from the post-processing regarding soot temperature and volume fraction, and shows that the radiative feedback evaluation from both methods should be consistent.

1. Introduction

Long lasting power supplies are needed for long term journeys into space, such as the Mission to Mars. Consequently, hazards associated with short-circuiting are enhanced. This makes the control and therefore the understanding and the prediction of potential flame spread over electrical wires crucial to spacecraft fire safety.

Flame spread over the coating of electrical wires in microgravity has been studied extensively [1–3]. Investigating concomitant flame spreads over three parallel Low Density PolyEthylene (LDPE) coated wires in microgravity, Citerne et al. [3] highlighted the major role of radiative transfer between neighboring flames, which especially lead to a significant acceleration of the central flame that could not be detected in normal gravity.

A recent numerical study by Guibaud et al. [4] focused on the structure of the axisymmetric flame spreading at a steady rate in an opposed oxidizer flow over the LDPE coating of a single NiCr core wire in microgravity. About two thirds of the radiative heat feedback from the flame to the burning material were attributed to soot particles. Solving the Radiative Transfer Equation (RTE), the spatial distribution of the radiative heat feedback along the wire surface could also be accessed. Given the high sensitivity of the polyethylene pyrolysis pathways to heating characteristics [5], assessing this distribution may represent a meaningful improvement towards the fine prediction of flame spread rate.

This simulation was validated against experimental measurements of soot

3

temperature and volume fraction in the non-buoyant flame of interest. The Broadband Modulated Absorption/Emission (BMAE) technique was developed to this end, first on a well documented buoyant laminar coflow non-premixed flame [6], then on the actual configuration simulated [7].

Herein, the fields computed by the aforementioned simulation are introduced together with the optical setup designed to probe the flame. The potential processings that this setup enables, i.e. those associated with the BMAE and the Broadband Two Color Pyrometry (B2CP), are then briefly outlined. As an original contribution, the signal modeling that underlies these techniques is used to generate from the numerical fields the synthetic signals that the BMAE camera is expected to capture. These signals are then contrasted with the actual ones to assess the consistency of the optical design. Subsequently, the performances of both BMAE and B2CP approaches are explored, especially in terms of soot-related radiative feedback evaluation, knowing that the implementation of the B2CP technique is more compact [8], therefore more embeddable.

2. Investigation configuration

2.1. Flame features

Figure 1 displays the fields of soot volume fraction (f_v) and temperature (T) within a flame spreading in a laminar opposed flow over the LDPE coating of a NiCr core electrical wire in microgravity. Thus, the configuration is axisymmetric. The radial distance from the wire's axis and the streamwise coordinate along this axis are referred to as r and z, respectively. In addition, the flame spread rate is steady and the fields are represented in the frame of
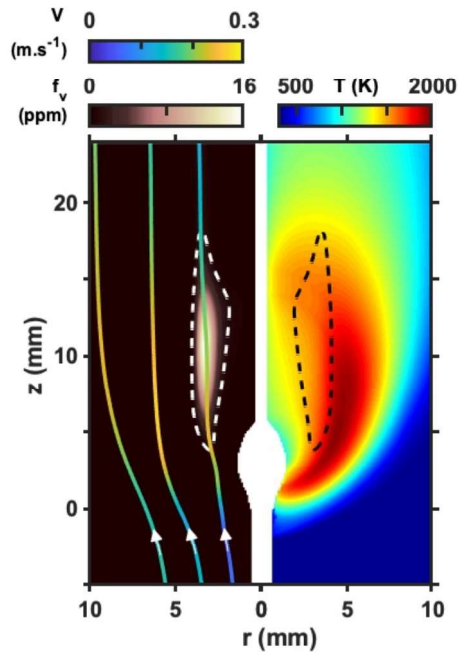
4

Figure 1: Fields obtained by numerical simulation of soot volume fraction f_v (left) and temperature T (right) in a flame spreading in an opposed flow over the LDPE coating of an electrical wire in microgravity (ambient pressure P=1013 mbar, free stream velocity V_∞=200 mm.s^{-1}, oxygen content of the oxidizer X_{O_2}=0.21). The dotted lines encompass the zone producing 95% of the radiative power attributed to soot. The axisymmetric wire is represented by the white area along the wire's axis (r=0). The color of the streamlines drawn on the left indicates the magnitude of the flow velocity field V.

the flame.

These fields were computed by a numerical simulation [4]. The numerical model used some experimental measurements as input data, among which the wire's profile and the spread and pyrolysis rates. The model then solved steady-state transport equations for mass, momentum, species, energy, and soot number density and mass fraction in conjunction with a state-of-the-art
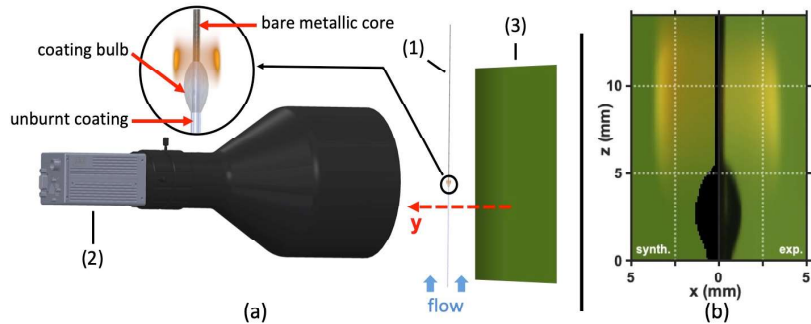
Figure 2: (a) Schematic of the arrangement allowing the flames spreading in microgravity to be probed by the BMAE technique. Only the main items are identified: (1) wire over which the flame is spreading downwards in an opposed flow; (2) camera mounted with a telecentric lens; (3) backlighting screen. The inset displays a close-up on the spreading flame. (b) Half-frames of the experimental flame (on the right of the projected wire's axis $x=0$) captured by the setup and the synthetic flame (on the left) computed from the fields shown in Fig.1 as the backlighting is on.

radiation model accounting for both gaseous species and soot contributions. Details of the simulation and those of the numerical methods can be found in Refs. [4] and [9].

This simulation was validated against soot temperature and volume fraction measured by the BMAE technique [4]. Using the Detection of Ignition And Mitigation Onboard for Non-Damaged Spacecrafts (DIAMONDS) rig extensively detailed in Ref. [3], the experiments were conducted aboard the Novespace A310 ZeroG airplane that specifically operates parabolic flights. Every parabola provides a 22 s long sequence of microgravity with an accuracy of 10^{-2} g_0 (g_0=9.81 m.s^{-2}). The flame investigated was shown to propagate at a steady rate within the ultimate 5 s of the parabola [4].

The soot volume fraction field simulated was consistent with the experi-

mental one in terms of shape and maximum value [4]. Nevertheless, the model underestimated soot oxidation, leading to a longer computed soot layer. As illustrated by the contour in Fig.1, the region where the soot content is high enough to produce a signal that the BMAE can exploit experiences a relatively low temperature gradient. However, the soot temperature measured by the BMAE within this region was decently captured by the numerical simulation. The computations also showed that soot radiation dominates the radiative heat transfer in this flame, contributing for about two thirds of the total radiation. This echoed for the first time on this specific configuration that radiation from soot can play a major role in the heat transfer involved in non-buoyant flame spread, even for small non-premixed flames [10]. As a matter of fact, the rightmost streamline shown in Fig.1 flows through the location of the peak soot volume fraction and experiences a maximum velocity magnitude of 0.25 m.$^{-1}$. As compared to the equivalent buoyant flame where velocities higher than 1 m/s occur, the moderate acceleration that is here strictly attributed to thermal expansion leads to expanded time scales associated with transport and combustion processes, increasing soot concentration [11] and radiative emissions [12].

2.2. Optical diagnostics

Figure 2(a) displays a schematic of the main devices enabling the BMAE technique. The flame investigated can be probed with this kind of relatively compact setup by non-intrusive energy levels of light [7]. In turn, such a technique requires relatively long line-of-sight to get a decent signal-to-noise ratio, therefore needs to be combined with a deconvolution procedure to retrieve the local information. The BMAE setup was cautiously shown to

7

allow for the measurements of both local soot temperature and volume fraction fields with uncertainty levels that do not exceed ± 50K and ± 0.5 ppm, respectively [6]. Only the key features of the technique are reminded in the following.

Images of the spreading flame (1) are captured using a digital 12-bit tri-CCD camera (2), equipped with a 100 mm diameter telecentric lens to restrict the light collection to beams parallel to the optical axis y. Light is collected by the three 512x1396 pixels^2 CCD arrays over three spectral bands, ranging from 400nm to 510nm (blue), 480nm to 600nm (green), and 570nm to 700nm (red), respectively. The spectral sensitivity over each band together with the setup transmissivity have been carefully established using a monochromator, allowing for the evaluation of the transfer function f_λ required by the signal processing. Pixel resolution of the projected data is 72.6 μm for each spectral band, and images are acquired at a rate of 39.06 fps.

Images of the flame with and without a backlighting are then required. As a result, both the sample to be burnt and a backlighting screen (3) are aligned on the camera optical axis. To generate such a backlight that uniformly illuminates the sample, the light delivered by four sets of blue, green, red, and white LEDs is reflected on a white diffusive screen. This backlighting is alternatively set on and off by a digital pulse generator that also triggers the start of the CCDs exposure. Thus, the sequence of frames recorded by the frame grabber along the microgravity period of time consists of a set of pairs (typically 500), each imaging consecutively the flame with and without the backlight.

The current powering each of the aforementioned four sets of LEDs can

be adjusted independently. The dynamics of the blue, green, and red signals can then be optimized for every set of experimental conditions. Typically, for every spectral range, about 2,000 levels of intensity (a.u.) are devoted to the measurements of the mean backlighting intensity and its partial absorption through the flame while the flame emission is captured when the backlighting is off over the remaining part ($\sim$2,095 levels). A typical frame recorded as the backlighting is on is shown in Fig.2(b) on the right of the projected wire's axis (x=0).

2.3. Data processing

BMAE. To interpret the signal conveyed on each pixel of such a frame, the RTE in its non-scattering formulation is integrated along a straight light beam crossing the axisymmetric flame (see the y-axis in Fig.2). The energy per unit time impacting a pixel at a given wavelength λ over a bandwidth $d\lambda$ scales as follows [6]:

$$d\mathcal{E}_\lambda \sim \left(\int_{y_m(x)}^{y_M(x)} (\kappa B)_\lambda(y) \, e^{-\int_y^{y_M(x)} \kappa_\lambda(y')dy'} \, dy + \phi_\lambda \, e^{-\int_{y_m(x)}^{y_M(x)} \kappa_\lambda(y')dy'} \right) d\lambda$$

(1)

where ϕ_λ is the intensity per unit area of the backlighting in the absence of the flame. The second term between parentheses in Eq.(1) quantifies the intensity attributed to the backlighting that is partially attenuated through the flame due to the field of local spectral absorption coefficient κ_λ. The first term is the contribution cumulated along the line-of-sight of the flame local spectral emission rate $(\kappa B)_\lambda$, B_λ being the spectral blackbody radiative intensity given by Planck's law. This term also accounts for absorption along

9

the line-of-sight in the exponential factor.

The total intensity $\mathcal{E}$ collected by a pixel of each broadband CCD sensor is the result of the accumulation over the spectrum of $d\mathcal{E}_\lambda$ weighed by the transfer function f_λ of the sensor:

$$\mathcal{E} = \int_\lambda f_\lambda \, d\mathcal{E}_\lambda \tag{2}$$

The flame investigated spreads at a rate of about 1mm.s^{-1} [7], which means that between two consecutive frames the flame shifted of about 25μm, i.e. 0.3 pixel. As such, and given the smooth variations of the soot distribution in the streamwise direction, the spread rate can be considered slow enough to leave the first term of Eq.(1) unchanged from one frame capturing the flame as the backlighting is on to the subsequent one as it is switched off [6].

As outlined by Guibaud et al. [6], at every line (z) along the wire's axis, two successive deconvolutions are required to recover first κ_λ, then B_λ. The integrals in Eq.(1) are spatially discretized. Doing so, an onion-peeling method combined with a Tikhonov regularization can be conducted for every deconvolution and the field of interest is retrieved iteratively from the outer layers towards the axis of the flame.

Due to the spectral integration (see Eq.(2)), an additional iterative procedure is required. At the initial step for the line considered, κ_λ is obtained for λ centre of the spectral band. A first guess of the soot volume fraction profile is obtained using the Rayleigh limit of the Mie Theory applied to soot particles expressed as follows:

$$\kappa_\lambda = \frac{6\,\pi\,E(m_\lambda)}{\lambda} f_v \tag{3}$$

10

where $E(m_\lambda)$ is a function of the complex refractive index m_λ of soot. The model of m_λ by Chang and Charalampopulos [13] is selected for the present study, as discussed by Guibaud et al. [4]. Then the second term in Eq.(1) can be evaluated at every nanometer within the spectral band. Consequently, the integral of this term over the bandwidth (see Eq.(2)) is computed. The discrepancy with the profile measured is finally used to predict the adjustment of the f_v profile for the next iteration.

κ_λ being obtained, the field of B_λ, therefore T, can be inferred from the emission field. The setup collection efficiency being unknown, the absolute emission cannot be quantified. Consequently, temperature is found from the signal ratio of flame emission within two different spectral ranges, i.e. the green and the red ones. Following an iterative procedure similar to that leading to each f_v profile, the temperature profile that generates numerical ratios closest to the experimental ones is retained. It is worth reminding that the complex impact of temperature on the value of the ratio leads to a more careful numerical optimization (see Ref.[4] for details).

B2CP. Widely used, the optically-thin flame approximation leads to ignore the effect of absorption along the line-of-sight. The subsequent evaluation of the energy per unit time impacting a pixel can then be scaled as follows in the absence of any backlighting:

$$d\mathcal{E}_\lambda \sim \left(\int_{y_m(x)}^{y_M(x)} (\kappa B)_\lambda(y)\, dy \right) d\lambda \tag{4}$$

In such a configuration, the B2CP technique can readily be implemented. Interestingly, this technique can be considered a simplified version of the BMAE one. With regard to the experimental setup required, the backlighting

11

shown in Fig.2(a) can be removed and the remaining devices used as they stand.

Although quite similar, the sequence of the retrieval processing is then reversed [8]. The temperature field needs to be retrieved first. To this end, Eq.(4) is solved twice for the fields of measurements $M_\lambda \sim S^p \eta_\lambda (\kappa B)_\lambda$ at two different spectral ranges λ_1 and λ_2. Provided a model for the spectral dependence of $E(m_\lambda)$ in Eq.(3), the ratio of both fields leads to the local temperature as follows [8]:

$$T \approx \frac{h\,c}{k} \frac{\lambda_1^{-1} - \lambda_2^{-1}}{log\left(\frac{M_{\lambda_1}}{M_{\lambda_2}} \frac{E(m_{\lambda_2})}{E(m_{\lambda_1})} \frac{\lambda_2^6}{\lambda_1^6} \frac{\eta_1}{\eta_2}\right)} \tag{5}$$

By analogy with the broadband computations prescribed for the BMAE processing, the spectral integral of the signal can be evaluated following Eqs.(4) then (2) and the temperature field inferred iteratively.

At this point, the field B_λ is computed and Eq.(4) is solved once more to retrieve κ_λ, therefore f_v. Again, an ultimate iterative procedure to account for the spectral integration of the signal allows the evaluation of T, and then f_v, to be refined.

3. Results and discussion

In the following, the outputs extracted from the original numerical simulation, the synthetic procedure, and the experimental one are identified by the subscripts o, *synth*, and *exp*, respectively.

3.1. Optical design consistency

Figure 2(b) displays the contrast between the experimental frame and the synthetic one, shown on the right and on the left side of the projected
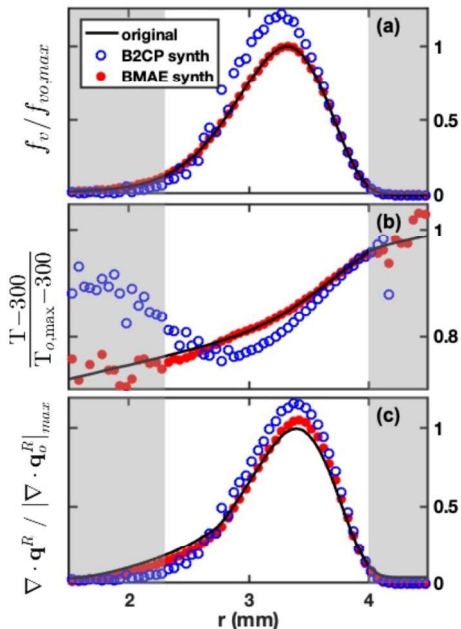
Figure 3: Profiles at z=10.8mm of: (a) soot volume fraction; (b) temperature; (c) radiative balance. The quantities are scaled by their peak values within the original fields shown in Fig.1 ($f_{vo,max}$=15.7ppm, $T_{o,max}$=1961K, $\left|\nabla \cdot \mathbf{q}_o^R\right|_{max}$=39.5kW.m^{-3}). The white stripe represents the region producing 95% of the radiative power attributed to soot.

axis (x=0), respectively. The latter was computed line by line along the z coordinate. For every line, the inputs are the profiles of both soot volume fraction and temperature extracted from the fields shown in Fig.1. For every CCD sensor of the camera, a set of narrow spectral bands is selected to enable the numerical integration over the sensor's sensitivity bandwidth (see Eq.(2)). For every narrow band, the profiles of κ_λ and B_λ can be computed following Eq.(3) and Planck's law, respectively, then processed following the discrete formulation of Eq.(1).

To scale the synthetic signals over 12 bits, only the peak synthetic red

intensity in the absence of backlighting together with the red intensity of the backlighting in the absence of the flame were adjusted to the corresponding experimental values. The other two intensity ranges, i.e. the blue and the green ones, are then set by the actual transfer functions f_λ that have been caustiously measured [6].

As a matter of fact, the topology of the synthetic frame in both shape and color is very close from the experimental one. More specifically, the flame standoff distance appears to be decently captured. The evolution along the streamwise coordinate of this quantity is governed by the coupling between the heat transfer from the flame to the burning material and the mass transfer in the opposite way [14]. As such, the optical design is here supported by a fine agreement of the expected signals with those produced by the experimental flame.

That being said, the synthetic flame is slightly longer than the experimental one. This is due to the weaker rate of soot oxidation at the flame trailing edge as identified by Guibaud et al. in their numerical simulations [4].

3.2. Soot temperature and volume fraction

Starting from the synthetic frame shown in Fig.2(b), both the BMAE and the B2CP techniques can be implemented to retrieve the fields of local soot temperature and volume fraction (see details in Part 2 of the Supplemental material S1). Especially because the quantities that are first retrieved are different, i.e. soot volume fraction for BMAE and soot temperature for B2CP, a given level of noise added to the synthetic frame does not affect the performances of the techniques in a comparable way. For this reason, only

14

the native noise that is due to the analogic to digital conversion is included to the synthetic signals, as outlined in the former Section.

To assess the capacity of both BMAE and B2CP techniques to retrieve the aforementioned fields, the profiles of soot volume fraction and temperature are shown in Fig.3(a) and (b), respectively. The original peak soot volume fraction throughout the flame is met at the height selected (z=10.8 mm). Thus, the level of expected signals is relatively high over the profiles processed. As a result, the spatial domain over which the performances of the techniques are expected to be fine is relatively wide. As an illustration, the white stripe in Fig.3 represents the region that produces 95% of the radiative power attributed to soot, also delineated by the contours shown in Fig.1.

As extensively explained by Guibaud et al. [6] for a buoyant coflow ethylene/air flame, the onion-peeling method proceeds from the outer to the inner layers, which results in the accumulation of the potential error along the deconvolution. This especially leads to poor performances of the temperature retrieval at the vicinity of the axis (see the left shaded region in Fig.3(b)) while the discrepancies in term of soot volume fraction in this region are smoothed by the large scale required on the y-axis of Fig.3(a).

Over the white stripe, both profiles of soot temperature and volume fraction are finely retrieved by the BMAE technique, as expected due to the signal modeling that specifically underlies the methodology associated with the BMAE technique. Meanwhile, the local flame intensity scaling as $\int K_\lambda B_\lambda d\lambda$ is not corrected for soot self-absorption by the B2CP processing and the temperature profile is then underestimated gradually towards the axis due
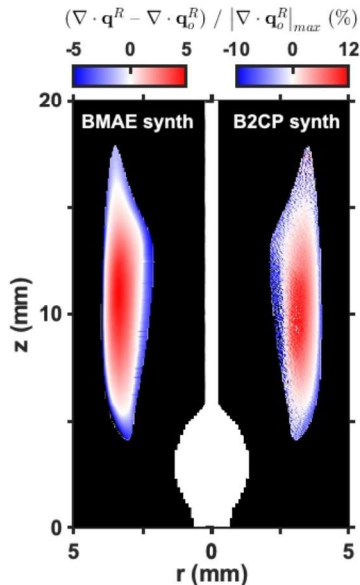
15

Figure 4: Fields of relative radiative balance discrepancy. $\nabla \cdot \mathbf{q}_o^R$ is computed from the fields shown in Fig.1. The fields of soot temperature and volume fraction retrieved by synthetic BMAE and B2CP are used to compute $\nabla \cdot \mathbf{q}^R$ on the left and on the right of the wire's axis, respectively. Only the region that produces 95% of the radiative power attributed to soot is mapped. ($\left.|\nabla \cdot \mathbf{q}_o^R|\right|_{max}$=39.5 MW.m^{-3})

to the accumulation of the error attributed to this absorption. At a level of expected $\int K_\lambda B_\lambda d\lambda$, this trend leads to a compensation through the evaluation of K_λ, i.e. soot volume fraction. As a result, the peak soot volume fraction retrieved by B2CP is overestimated by approximately 20%.

3.3. Radiative heat transfer computations

Using a temperature field and a soot volume fraction one as inputs, the RTE can be solved in its non-scattering formulation for the radiative intensity I_λ using the Finite Volume Method proposed by Chui et al. [15] for axisymmetric coordinates with a 12x16 angular mesh. Further angular refinement

16

did not lead to any significant evolution of the computed outputs. At every location in the field, the local radiative balance $\nabla \cdot \mathbf{q}^R$ can then be computed together with the radiative flux attributed to soot that is incident to the wire surface [7] (see details in Part 1 of the Supplemental material S1).

Figure 3(c) displays the profiles of radiative balance at z=10.8 mm. The fields produced by both synthetic BMAE and B2CP techniques allow the original profile to be decently captured. Still, the B2CP data lead to a significant overevaluation at the peak and a substantial underestimation at the inner side. These trends also reveal for the BMAE data at the lower extent.

Highlighting this topological similarity, Fig.4 maps the discrepancies of the radiative balance throughout the region encompassed in the contour shown in Fig.1. In addition, the field obtained with the B2CP data appears more uneven at the flame trailing edge (z >15 mm). This is especially due to the amplification by the B2CP processing of the error associated with the omission of soot self-absorption, as illustrated in Fig.3(b) around r=2.2 mm in a region of lower $\nabla \cdot \mathbf{q}^R$, i.e. lower expected signal. Interestingly, for both BMAE and B2CP, the central part of the flame is dominated by an overestimation of $\nabla \cdot \mathbf{q}^R$, which is balanced to some extent by an underestimation in the surrounding region.

Figure 5(b) shows the incident radiative flux attributed to soot at the wire surface for the conditions investigated so far. Due to the bulb profile reported on the left, the local view factor between the surface and the flame exhibits an upstream peak located at z=5.3 mm [4]. Concomitantly, the region of higher radiative power reveals downstream around z=11 mm. Under both
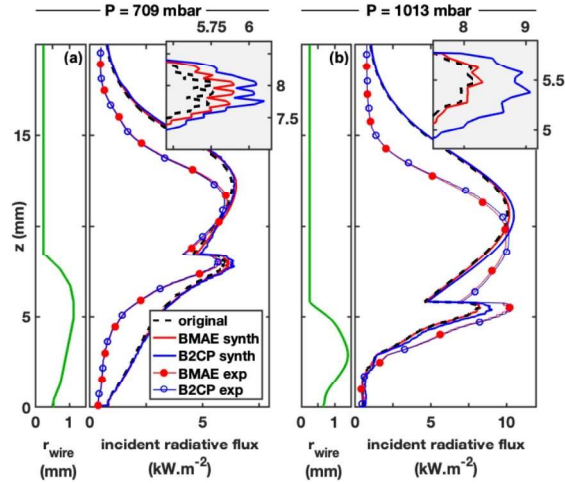
17

Figure 5: Profiles along the wire of the incident radiative flux attributed to soot for (a) P=709 mbar and (b) P=1013 mbar, the velocity and the oxygen content of the oxidizer being kept constant. The profile of each burning wire is displayed on the left. Each inset highlights the deviations at the synthetic peak flux located on the coating bulb. The peak optical thickness for the red spectral range is 0.09 and 0.38 for conditions (a) and (b), respectively.

effects, every profile of incident radiative flux exhibits two peaks along the wire.

The inset in the upper right corner highlights the discrepancies among the profiles at the peak facing the bulb. While the flux obtained from the synthetic BMAE data exhibits a weak deviation from that given by the original data, even the peak flux inferred from the synthetic B2CP data leads to a difference that does not exceed 10%. Consequently, in the best case scenario of the present configuration, i.e. in the absence of substantial noise, the enhancement in discrimination capacity provided by the BMAE technique as compared to the B2CP one is not meaningful.

18

It is worth noticing here that at this peak the better agreement between the BMAE and the B2CP over the experimental fields is a consequence of the thinner radial distribution of soot volume fraction in the experimental evaluation, which reduces self-absorption effects.

This is further assesed by the profiles obtained from the experimental BMAE and B2CP data. While the location of the downstream experimental peak is shifted upstream due to the longer soot layer numerically reproduced, its magnitude is fairly well captured. In contrast, the locations of the upstream peaks merge but their magnitudes differ. This is especially due to the peak soot volume fraction that occurs further downstream in the numerical simulation [4]. That being said, both experimental BMAE and B2CP profiles can be hardly discriminated as expected in the light of the above synthetic approach.

As an ultimate evidence of the similar performances conferred to both techniques, the whole procedure was reproduced for P=709 mbar (see Fig.5(a)). Due to the significantly lower amount of soot in this flame ($f_{v,max}$=5.0 ppm), the magnitude of the profiles is substantially decreased. Furthermore, the discrepancy between the synthetic BMAE and B2CP profiles almost vanished, what is confirmed by the experimental profiles.

4. Conclusions

Within the context of a non-buoyant axisymmetric flame propagating in an opposed laminar oxidizer stream over the LDPE coating of an electrical wire, non-intrusive optical measurements of soot temperature and volume fraction were proven to lead to a proper evaluation of the incident radiative

19

flux attributed to soot along the surface of the wire. In addition, these measurements can be conducted without any significant loss of accuracy by the B2CP technique, i.e. in the absence of any absorption field evaluation. This new insight is especially guaranteed by the weak effect of absorption over the line-of-sight of every signal that drives the retrieval method, i.e. the intensity captured by a tri-CCD camera. The robustness of the present assessment is further strengthened by the original second set of experimental and numerical data, i.e. those for P=703 mbar (see Fig. 5(a)).

It is worth mentioning that the BMAE technique allowed the evaluation of the aforementioned effect, therefore the estimation of the discrepancy that can be attributed to the omission of the signal absorption. Moreover, the measurements of more local information, such as peak soot volume fraction or temperature, are significantly improved by the incorporation of the absorption effect to the signal interpretation, what the BMAE technique inherently includes.

Eventually, the entire study was undertaken with a single model for the spectral dependency of the soot refractive index. While the models available in the literature exhibit relatively large scattering, most of them agree on the relative tendency over the spectrum [16]. As a result, the relevance of the above insights are not expected to be affected by this still unclear input. Nonetheless, the interpretation of the measurements provided by the lower spectral range of the BMAE camera, i.e. the blue channel, might help clarify this issue, as already done on a buoyant coflow flame [17].

Acknowledgments

References

[1] M. Kikuchi, O. Fujita, K. Ito, A. Sato, T. Sakuraya, Experimental study on flame spread over wire insulation in microgravity, *Proc. Combust. Inst.* 27 (1998) 2507–2514.

[2] M. Nagachi, F. Mitsui, J.-M. Citerne, H. Dutilleul, A. Guibaud, G. Jomaas, G. Legros, N. Hashimoto, O. Fujita, Can a spreading flame over electric wire insulation in concurrent flow achieve steady propagation in microgravity?, *Proc. Combust. Inst.* 37 (2019) 4155–4162.

[3] J.M. Citerne, H Dutilleul, K Kizawa, M Nagachi, O Fujita, M. Kikuchi, G. Jomaas, S. Rouvreau, J.L. Torero, G. Legros, Fire safety in space – Investigating flame spread interaction over wires, *Acta Astronaut.* 126 (2016) 500–509.

[4] A. Guibaud, J.L. Consalvi, J.M. Orlac'h, J.M. Citerne, G. Legros, Soot production and radiative heat transfer in opposed flame spread over a polyethylene insulated wire in microgravity, *Fire Technol.* (2019), doi:10.1007/s10694-019-00850-82.

[5] S. Lovett, F. Berruti, L.A. Behie, Ultrapyrolytic upgrading of plastic wastes and plastics/heavy oil mixtures to valuable light gas products, *Ind. Eng. Chem. Res.* 36 (1997) 4436–4444.

[6] A. Guibaud, J.M. Citerne, J.M. Orlac'h, O. Fujita, J.-L. Consalvi, J.L. Torero, G. Legros, Broadband modulated absorption/emission technique to probe sooting flames: Implementation, validation, and limitations, *Proc. Combust. Inst.* 37 (2019) 3959–3966.

[7] A. Guibaud, J.M. Citerne, J.L. Consalvi, O. Fujita, J.L. Torero, G. Legros, Experimental evaluation of flame radiative feedback: methodology and application to opposed flame spread over coated wires in microgravity, *Fire Technol.* 28 (2019) doi:10.1007/s10694-019-00853-5.

[8] B. Ma, S. Cao, D. Giassi, D.P. Stocker, F. Takahashi, B.A.V. Bennett, M.D. Smooke, M.B. Long, An experimental and computational study of soot formation in a coflow jet flame under microgravity and normal gravity, *Proc. Combust. Inst.* 35 (2015) 839–846.

[9] H. Guo, F. Liu, G.J. Smallwood, Ö.L. Gülder, Numerical study on the influence of hydrogen addition on soot formation in a laminar ethylene-air diffusion flame, *Combust. Flame* 145 (2006) 324–338.

[10] S.L. Olson, J.S. T'ien, Buoyant low-stretch diffusion flames beneath cylindrical PMMA samples, *Combust. Flame* 121 (2000) 439–452.

[11] C.M. Megaridis, B. Konsur, D.W. Griffin, Soot-field structure in laminar

soot-emitting microgravity nonpremixed flames, *Proc. Combust. Inst.* 26 (1996) 1291–1299.

[12] W. Kong, F. Liu, Numerical study of the effects of gravity on soot formation in laminar coflow methane/air diffusion flames under different air stream velocities, *Combust. Theory Modelling* 13 (2009) 993–1023.

[13] H. Chang, T.T. Charalampopoulos, Determination of the wavelength dependence of refractive indices of flame soot, *Proc. Roy. Soc. Lond. A* 430 (1990) 577–591.

[14] J.L. Torero, T. Vietoris, G. Legros, P. Joulain, Estimation of a total mass transfer number from the standoff distance of a spreading flame, *Combust. Sci. Technol.* 174 (2002) 187–203.

[15] E.H. Chui, G. D. Raithby, P. M. J. Hughes, Prediction of radiative transfer in cylindrical enclosures with the finite volume method, *J. Thermophys. Heat Transf.* 6 (1992) 605–611.

[16] J. Yon, R. Lemaire, E. Therssen, P. Desgroux, A. Coppalle, K.F. Ren, Examination of wavelength dependent soot optical properties of diesel and diesel/rapeseed methyl ester mixture by extinction spectra analysis and LII measurements, *Appl. Phys. B* 104 (2011) 253–271.

[17] H. Zhao, B. Williams, R. Stone, Measurement of the spatially distributed temperature and soot loadings in a laminar diffusion flame using a Cone-Beam Tomography technique, *J. Quant. Spectrosc. Radiat. Transf.* 133 (2014) 136–152.
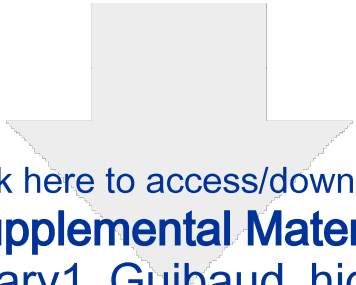
Click here to access/download
Supplemental Material
Supplementary1_Guibaud_highlighted.pdf